Chapter

Effect of Casting Processes, Rare Earth Metals, and Sr Addition on Porosity Formation in Al-Si Cast Alloys

Ehab Samuel, Agnes M. Samuel, Victor Songmene and Fawzy H. Samuel

Abstract

The present work was carried out on A413.1cast alloy that was characterized by short freezing temperature range. Measured amounts of high purity (99.99%) rare earth metals (Ce, La, La + Ce) were added to the non-modified and Sr-modified molten metal. Three casting molds were used viz., graphite mold heated at 600°C for the purpose of obtaining solidification curves, metallic mold with three variable opening angles heated at 350°C, and a step-like metallic mold heated at 200 and 400°C. The main results are earth metals (RE) would lead to porosity formation in all molds with increase in its percentage in Sr-modified alloys. Since the maximum α-Al network formation temperature is in the range of 575–580°C, some of the RE may precipitate in the liquid state leading to blocking the flow of the liquid metal. However, considering the metal was degassed using high purity argon gas, most of the observed porosities are of shrinkage type. In addition, increasing the amount of used RE, and hence percentage of unsoluble intermetallics results in marked decrease in the alloy strength. The only observed advantage is the effectiveness of La is reducing the alloy grain size due to its low affinity to react with Ti.

Keywords: casting process, rare earth metals, porosity formation, mold type, tensile properties

1. Introduction

The rare earth elements (REE) represent the 17 metallic elements in the periodic table with high atomic numbers (57–71). This series is composed of the 15 lanthanides on the periodic table in addition to Sc (21) and Y (39), which exist in the same ores containing the oxides of the REE/RE [1–4]. Most of the RE elements were named after the places where they were found or after the names of the scientists who discovered them. The term *'rare'* was used since these types of ores were never previously reported [5]. Although there are several extraction methods to produce individual

rare earth metal that have been described in the literature [6–9], little is published on their purity. It is stated that the purity of produced RE from their oxides falls between 88.5 [10] and 96.5% [11]. Also, the purity of RE depends on their prices due to the high cost of production [12].

During the past two decades, a fairly large number of articles have been published on the application of the rare earth metals La and Ce in Al-Si alloys. The authors claim that the addition of 0.2% of La or Ce produces significant modification of the eutectic Si particles [13–18], grain refining [19–21], and improvement in the alloy mechanical properties [22–24], which make RE very attractive for automotive industries. However, using high purity 99.99% La and Ce, Samuel and coworkers attributed the reported observations to the presence of tramp elements associated with the original ores and, thus, not necessarily caused by the added RE. In addition, the presence of a large volume fraction of RE-based intermetallics leads to severe deterioration of the alloy's mechanical properties [25–27]. Most of these studies were carried out on 356 alloys that were characterized by their long freezing range (6.5%Si). **Figure 1** shows a clear depression in the eutectic temperature of 356 alloys (like that reported for Sr addition [28]). However, the microstructure did not reveal a significant modification [29, 30] of the eutectic Si as claimed by the other authors.

The present work was carried out on A413.1 alloy to investigate the effect of the addition of different concentrations of La and Ce with and without Sr. This class of alloys is used for intricate thin-walled castings requiring pressure tightness, toughness, and good resistance to corrosion. The alloys have good machinability with carbide tooling. Aluminum A413. Zero is similar to Aluminum 413.0 except its iron content is lower than in A380 alloy. The 413 alloy is characterized by its short freezing range (~5°C at 0.8°C/s)). Hence, if the metal is well degassed, the only source of porosity is shrinkage porosity caused by mold geometry and temperature. To elaborate on this statement, three types of molds were used: a graphite mold (heated at 600°C), a variable angle metallic mold (heated at 350°C), and a step-like mold heated at 200°C and 400°C.

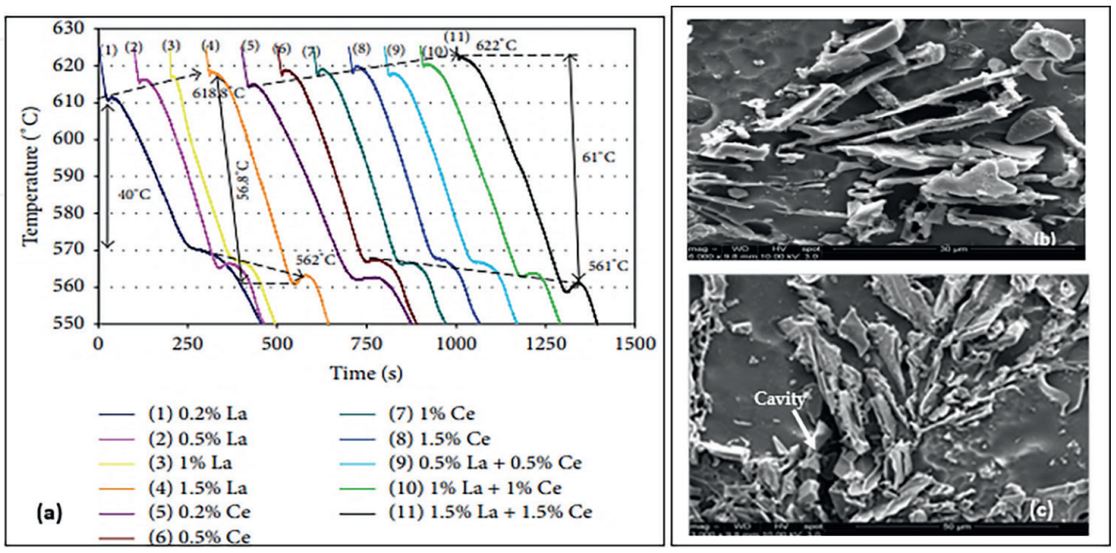

Figure 1.
Effect of addition of high purity La and Ce on the thermal behavior of 356 alloys (solidification rate of about 0.8°C/s), (b) alloy #1, (c) alloy #11. Note the absence of modification [28].

2. Experimental procedure

Table 1 lists the chemical analysis of the as-received 413 alloy. To obtain the solidification curves and to identify the main reactions and corresponding temperatures occurring during the solidification of the A413.1 alloy, thermal analysis was conducted for all the needed compositions to be prepared. The molten metal (using a 2-kg SiC crucible, heated to 750°C using an electrical furnace) for each composition was cast into a graphite mold preheated to 600°C to obtain a slow solidification rate resembling equilibrium conditions. A high-sensitivity Type-K (chromel-alumel) thermocouple was attached to the center of the graphite mold—**Figure 2(a)**; the temperature-time data was collected using a high-speed data acquisition system.

The ingots were melted in a 40 kg capacity SiC crucible using an electrical resistance furnace. The molten metal was degassed using pure, dry argon, and introduced into the melt using a graphite rotary impeller (at a speed of 130 rpm). Prior to degassing, measured amounts of Sr, La, and Ce were added. The three elements were introduced into the molten alloy in the form of Al-10%Sr, Al-20%La, and Al-20%Ce master alloys. At the end of the degassing period, the molten alloy was cast into two different molds, which provided different solidification rates:

1. A variable angle metallic mold (0◦, 5◦, and 15◦) heated at 350°C (**Figure 2(b)** and **(c)**).

2. A step-like metallic mold heated at either 200°C or 400°C (**Figures 2(d)** and **(e)**).

The melt was also poured into an ASTM B-108 permanent mold (preheated at 450°C to drive out moisture) for preparing the tensile test bar castings (gauge length of 70 mm and a crosssectional diameter of 12.7 mm). Tensile bars were solutionized at 510°C for 8 h, quenched in warm water at 60°C, and thereafter aged at 180°C for 2, 8, 20, and 50 h, followed by air cooling. All tensile bars were pulled to fracture using an MTS servo-hydraulic tensile testing machine at a strain rate of 4×10^{-4} s^{-1}. All bars were tested at 25°C, and each value represents the average of 10 tensile bars. The volume fraction of the precipitated intermetallics was determined using a JEOL JSM-6480LV scanning electron microscope coupled with an energy dispersive X-ray spectrometer (EDS) was used for examining the microstructures and semiquantitative analysis of the phases observed.

Table 2 summarizes the measured SDAS values obtained from the examined samples. Phase identification was carried out using an electron probe microanalyzer (EPMA) in conjunction with energy dispersive X-ray (EDX/EDS) analysis and wavelength dispersive spectroscopic (WDS) analysis where required, integrating a combined JEOL JXA-8900lWD/ED microanalyzer operating at 20 kV and 30 nA,

Alloy	Si	Mg	Mn	Cu	Fe	Sr	Ti	B
A413.1	11.17	0.14	0.218	0.71	0.344	0.0000	0.052	0.0003

Table 1.
Chemical composition of A413.1 alloy (% weight).

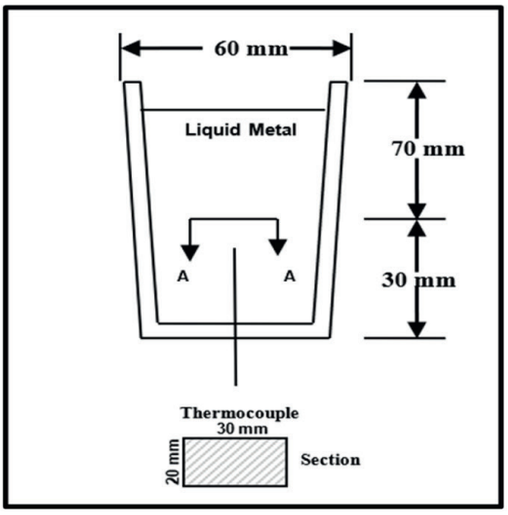

(a)

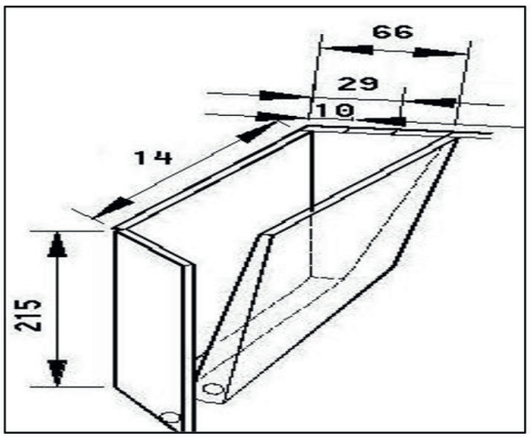

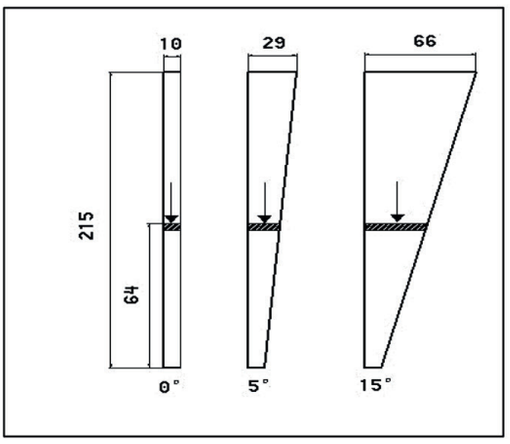

(b) (c)

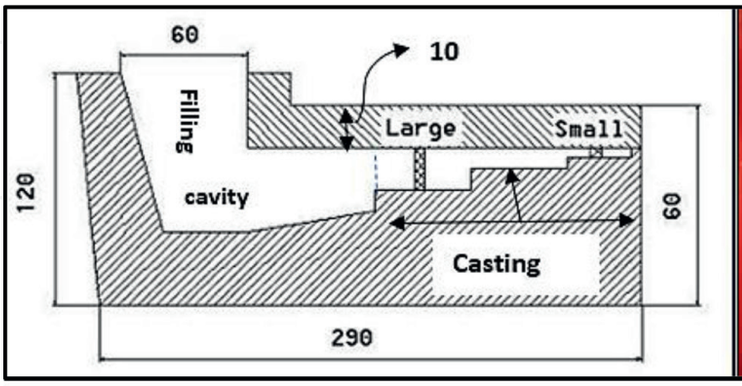

(d) (e)

Figure 2.
(a) Schematic of the thermal analysis setup. (b) Schematic of the metallic variable mold—all dimensions are in mm. (c) Sections from actual castings—arrows indicate samples position for metallographic examination. (d) Schematic of the step-like metallic mold (small 5 mm and large 20 mm) all dimensions in mm. (e) Actual mold and casting.

Mold	Mold temp. (°C)	Mold section	SDAS (μm)	
			Average	SD
Graphite	600	Center	68.63	5.49
	200	Large	31.56	2.92
Step-like	200	Small	16.17	1.89
	400	Large	41.66	3.02
	400	Small	22.46	3.96
Variable angle	325	Large	53.62	5.7
	325	Small	25.04	3.0

Table 2.
Average secondary dendrite arm spacing of the examined A356 alloy samples.

Aimed concentration (wt%)		Actual concentration (wt%)	
La	Ce	La	Ce
0.2	0	0.187	0
0.5	0	0.384	0
1	0	0.717	0
1.5	0	0.94	0
0	0.2	0.022	0.083
0	0.5	0.237	0.308
0	1	0.067	0.82
0	1.5	0.078	1.288

Table 3.
Aimed and actual La and Ce concentrations (weight%).

where the size of the spot examined was ~2 μm. **Table 3** summarizes the actual La and Ce concentrations using spectroscopic analysis. Average concentration of added Sr was in the range 150–180 ppm.

3. Results and discussion

3.1 Thermal analysis: graphite mold

Figure 3(a) depicts the solidification curve and its first derivative obtained from the base A413.1 alloy solidified at 0.8°C/s revealing a narrow solidification range of approximately 5°C compared to 43°C reported for the commercial A356.1 alloy as listed in **Table 4**. With the addition of 180 ppm Sr, the eutectic temperature in both alloys was dropped by about 7–8°C. In the absence of Sr, with the addition of La or Ce up to 1.5% (actual concentrations are reported in **Table 3**) the maximum drop in

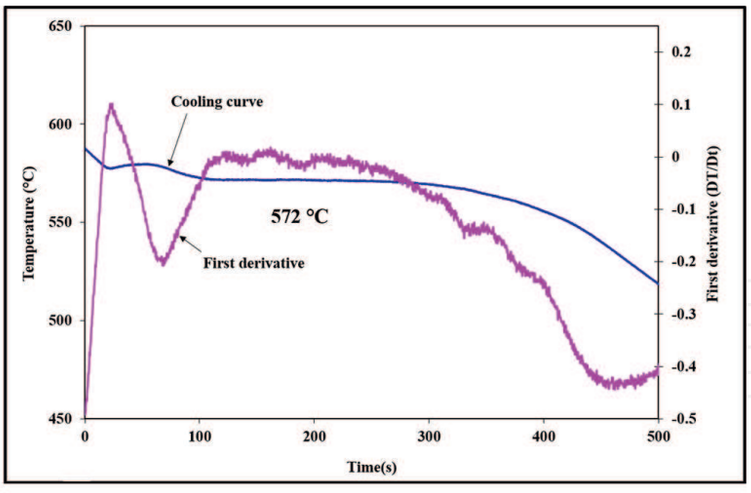

(a)

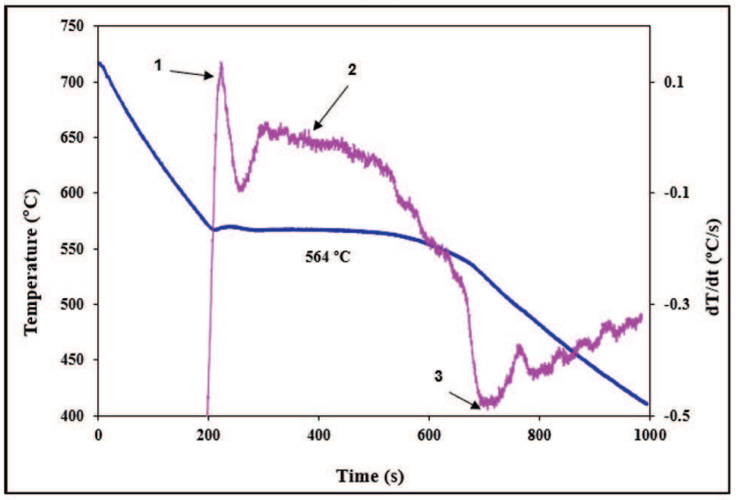

(b)

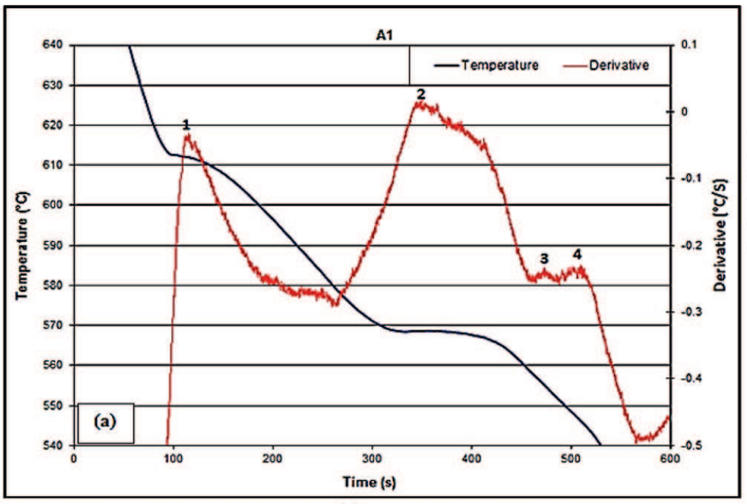

(c)

Figure 3.
Solidification curves and their first derivatives in: (a) base A413.1 alloy, (b) A413.1 alloy +180 ppm Sr, and (c) A356.1 alloy for comparison.

RE	α-Al (°C)	Al + Si (°C)	Freezing zone	ΔT (°C) increase in α-Al	ΔT (°C) decrease in Al + Si
0	577	573	4-5	0	0
Sr (180 ppm)	574	564	10	—	8
1.5 La	577	570	7	0	2
1.5 Ce	580	569	10	3	2
1.5 La +180 ppm Sr	574	565	9	—	7
1.5 Ce +180 ppm Sr	580	565	15	3	S
356 alloy	612	569	43		
356 allov+Sr	609	561	48		8

Table 4.
Effect of RE and Sr on the solidification characteristics of A413.1 alloy.

the eutectic temperature of A413.1 alloy is less than 2°C, taking into consideration that fluctuation in the solidification rate becomes more pronounced when the alloy is modified with Sr in addition to RE. According to Mahmoud et al. [28], the eutectic temperature can be expressed as:

$$T_R\,(\circ C) = 577 - 12.5\,w\mathrm{Si}\cdot(4.59\cdot w\mathrm{Mg} + 1.37\cdot w\mathrm{Fe} + 1.65\cdot w\mathrm{Cu} + 0.35\cdot w\mathrm{Zn} + 2.54\cdot w\mathrm{Mn} + 3.52\cdot w\mathrm{Ni}) \quad (1)$$

As can be seen, Sr was not taken into consideration. Based on this equation for the present alloy, T_R for A413.1 is about 574°C as reported in **Table 4**.

According to [31], both Al-La and Al-Ce reveal a eutectic reaction at low RE concentration as depicted in **Figure 4**. From **Table 4**, the addition of La or Ce up to 1.5% seems to have a marginal effect (3–4°C) on the two main reactions in A413.1 alloy, that is, precipitation of α-Al and (Al + Si) eutectic, increasing the freezing zone to 10°C. **Figure 5(a)** exhibits the effect of gradual addition of Ce on the temperature of the (Al + Si) eutectic reaction, reaching maximum 2–3°C at 1.5%Ce, which is due to the change in the alloy composition. The addition of 180 ppm Sr was proven to be more effective in reducing the (Al + Si) eutectic reaction by about 8–10°C as shown in **Figure 5(b)**, leading the total increase in the in the freezing zone to be 15–17°C compared to 45°C in the case of A356.1 alloy. Another point to be considered from **Figure 5(c)** is the appearance of undercooling for (Al + Si) curves treated with Sr (about 2–3°C) with no effect on undercooling associated with the precipitation of α-Al phase, which is apparently controlled by addition of grain refiners [32]. Also, increasing the Ce content between 0.5 and 1.5% has no independent effect as shown in **Figure 5(c)**.

Another important aspect to be discussed is RE-grain refiner interaction. According to the Hall-Petch relationship,

$$\sigma = \mathrm{K} + \mathbf{1}/\mathrm{d}^{1/2} \quad (2)$$

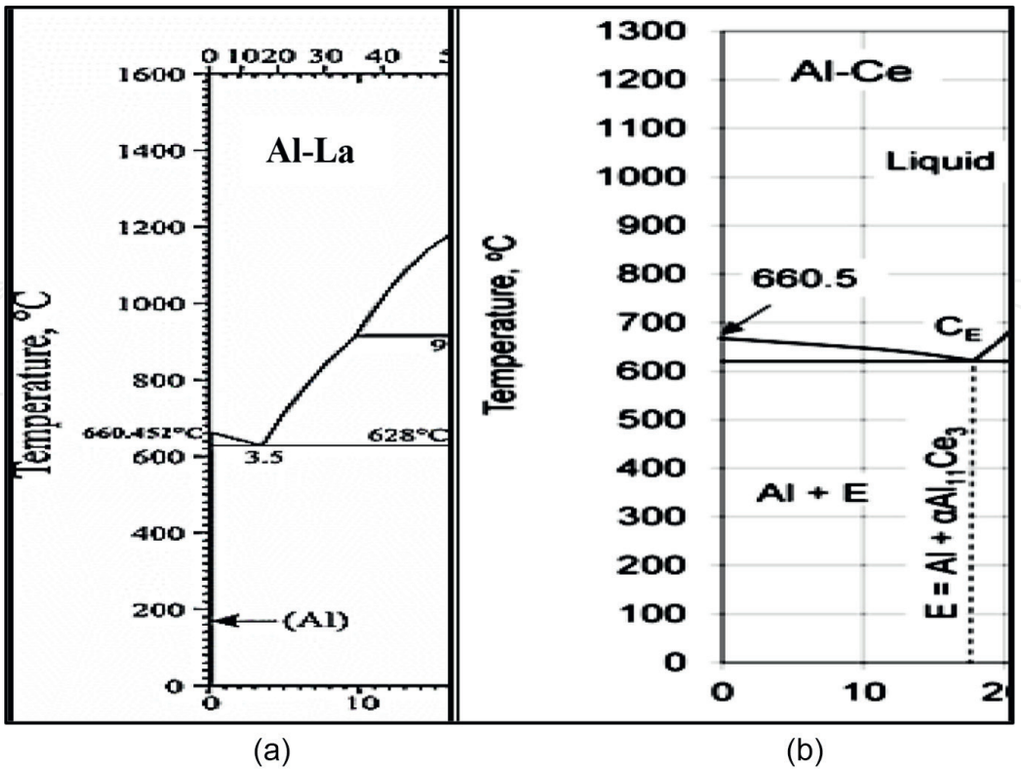

Figure 4.
Sections from (a) Al-La and (b) Al-Ce binary diagrams.

where σ = alloy strength, K is constant, and d is the average grain diameter. To emphasize this concept, the base alloy was grain refined with 0.12%Ti in the form of Al-5%Ti-1%B mater alloy added to the molten metal prior to degassing. Although the alloy originally contains 0.05%Ti in the form of TiBor, however, during remelting, the TiBor loses its effectiveness. The Ce-rich phase occurs in the form of gray compacted slugde or in star-like form (**Figure 6(a)** and **(b)**). Some authors [33–35] have defined an empirical factor (the "sludge factor"), given by:

$$\text{Sludge Factor} = (1\,X\%Fe) + (2\,X\%Mn) + (3\,X\%Cr) \tag{3}$$

When this factor becomes larger than a certain critical value, "sludge" may occur. All the elements are known as transition elements, which include Ti as well.

The X-ray distribution of Ce and Ti in one of the particles in **Figure 6(a)** are illustrated in **Figure 7(a)** and **(b)**, respectively, revealing strong intensity of Ti as confirmed by the associated EDS presented in **Figure 7(c)**, where the ratio of Ti/Ce is about 11.3/17.6 in weight % (approximately 65%). **Figure 6(c)** displays the precipitation of La-rich particles that are characterized by their shiny appearance and flat surface. As in the case of Ce, **Figure 8** reveals the X-ray distribution of La and Ti in one of the platelets in **Figure 6(c)**, where the white arrow is near the bottom of the intensity bar. The EDS pattern exhibited in **Figure 8(c)** reveals that the Ti concentration is almost 2% compared to La, which is about 40 (wt.%), that is, Ti/La is approximately 0.05%, which explains the absence of a Ti peak in the EDS spectrum.

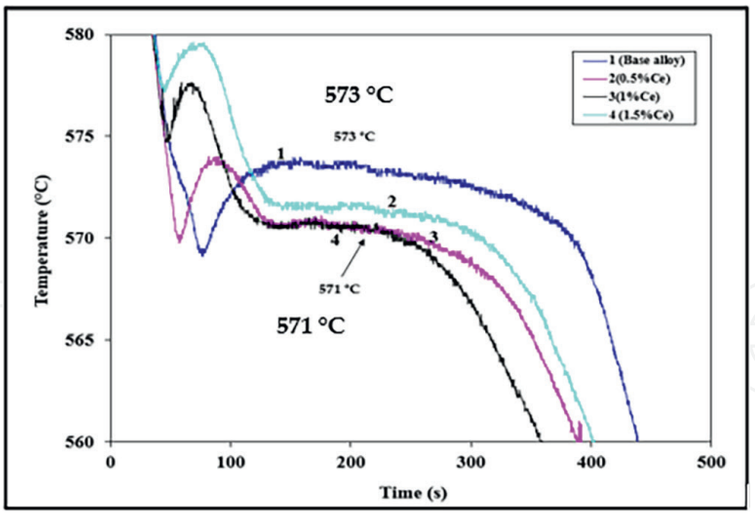

(a)

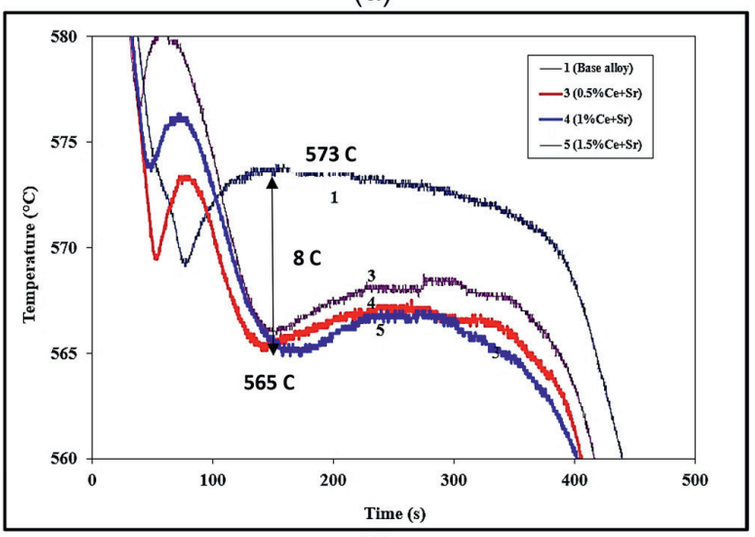

(b)

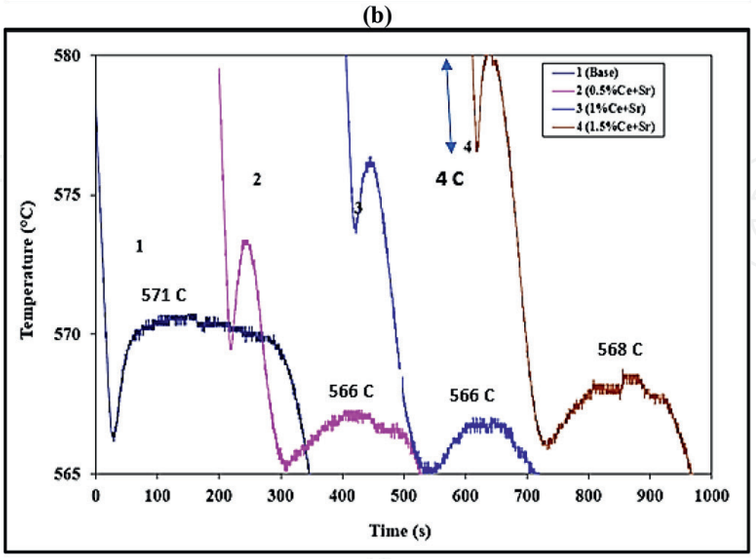

(c)

Figure 5.
(a) Effect of addition of Ce, (b) Ce + Sr on the solidification characteristics of A413.1 alloy, and (c) enlarged portions of (Al + Si) reactions in (b).

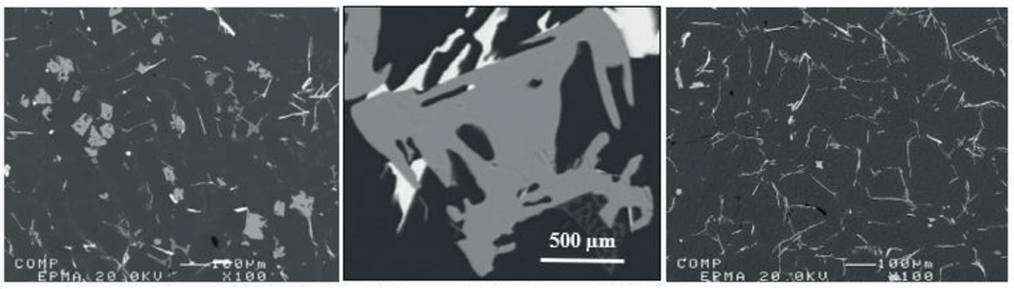

Figure 6.
Precipitation of RE intermetallics in A413.1 alloy containing: (a) 1.5%Ce; (b) high magnification image of (a); (c) 1.5%La.

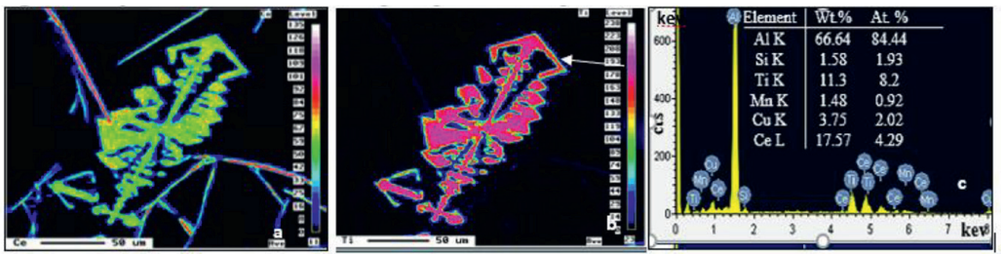

Figure 7.
X-ray images of (a) Ce, (b) Ti, (c) EDS spectrum showing the.

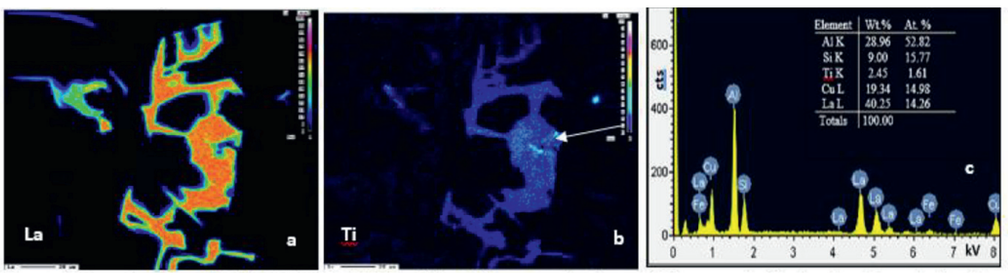

Figure 8.
X-ray images of (a) La, (b) Ti, (c) EDS spectrum showing the Ti and La concentrations.

Figure 9 shows a series of macrostructures revealing the variation in the grain size of A413.1 alloy as a function of the added Ti, La, and Ce. The average grain size of the as-received alloy was about 1850 µm (based on measuring about 100 grains using the line intercept method)—**Figure 9(a)**. Once the grain refiner was added, the average grain size was reduced to 750 µm (**Figure 9(b)**) indicating that 0.12%Ti is sufficient to refine the alloy grains. **Figure 9(c)** clearly shows the effect of Ce-Ti interaction; although the grain size was further reduced to 500 µm (**Figure 9(c)**), the combined addition of (La + Ti) resulted in a much finer grain size of about 370 µm (**Figure 9(d)**), representing 20% of the original grain size. The difference between grain size in **Figure 9(c)** and **(d)** represents the amount of Ti lost in interacting with Ce in the form of non-dissolvable intermetallics, which have a negative effect on the alloy mechanical properties, as depicted in **Figure 10** for Ce-rich intermetallics. **Figure 11** reveals a series of backscattered electron micrographs taken from the tested bars demonstrating the change in the size and distribution of the precipitated Al_2Cu phase particles, on going from fine rounded particles (**Figure 11(a)**), to short platelets (**Figure 11(b)**), to a mixture of thick platelets and spherical particles (**Figure 11(c)**)

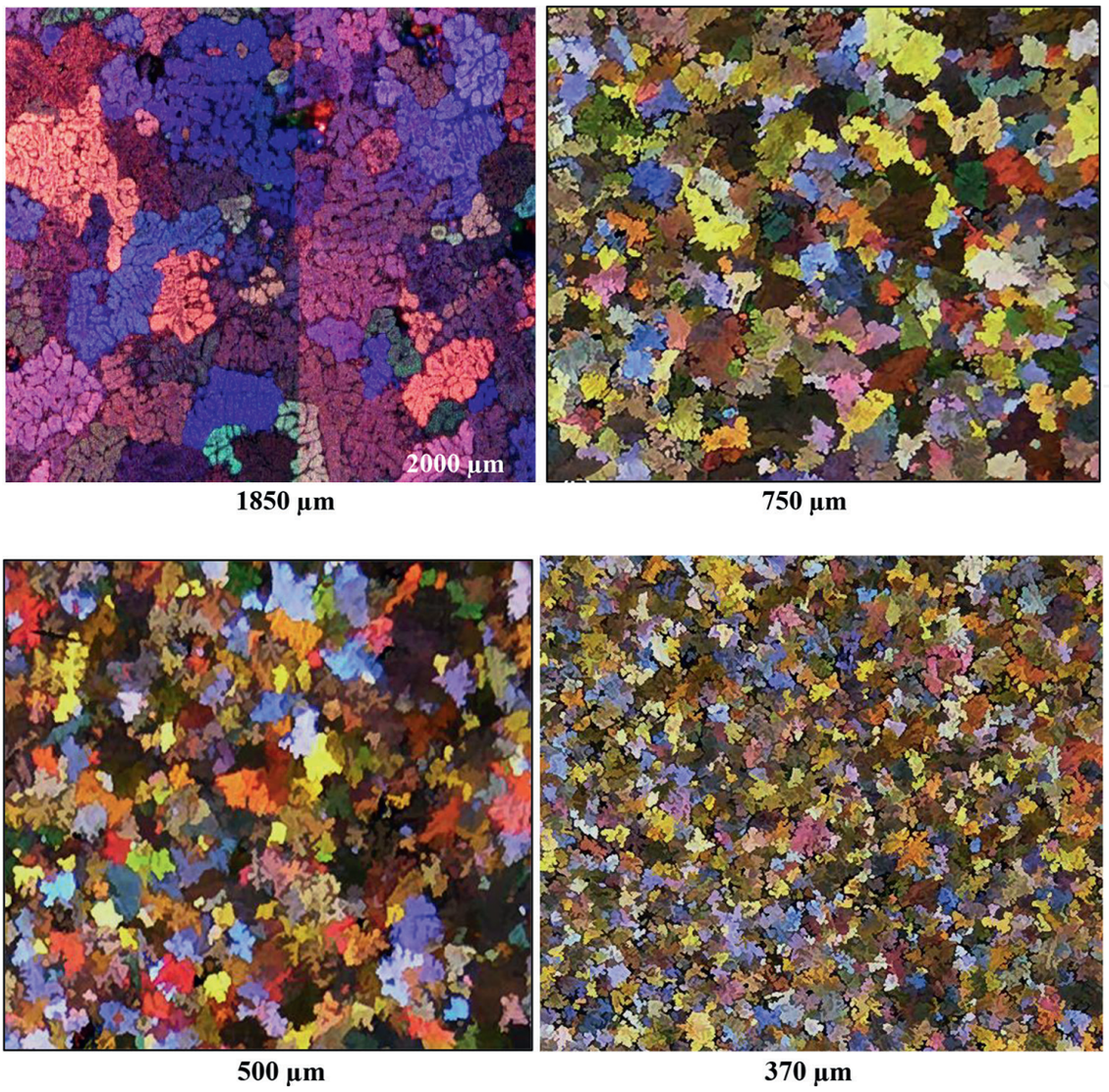

Figure 9.
Effect of grain refiner, Ce, and La addition on the alloy average grain size: (a) as-received alloy, (b) after addition of 0.12%Ti, and (c) Ti + Ce, (d) Ti + La.

indicating the beginning of incoherent precipitation. The EDS spectrum displayed in **Figure 11(d)** shows in addition to Al_2Cu particles, presence of Ce-rich intermetallics (gray phase in **Figure 11(c)**—orange arrows.

As mentioned in the experimental section, alloys for thermal analysis were not degassed due to the size of the used crucible, which reflected on porosity formation in the base alloy when RE was added. Since Ce-based phase particles precipitate in the form of star-like particles, their dendrite arms can be seen passing through the α- Al dendrite network as illustrated in **Figure 12(a)**, whereas La-rich platelets are observed lining the inner walls of the gas pores as demonstrated in **Figure 12(b)**.

3.2 Metallic variable mold

In this part, La, Ce, and La + Ce were added to the molten metal with and without Sr. **Figure 13(a)** demonstrates the occurrence of a hot zone in a small section toward the bottom of the mold (the first part to be filled with liquid metal). These zones are

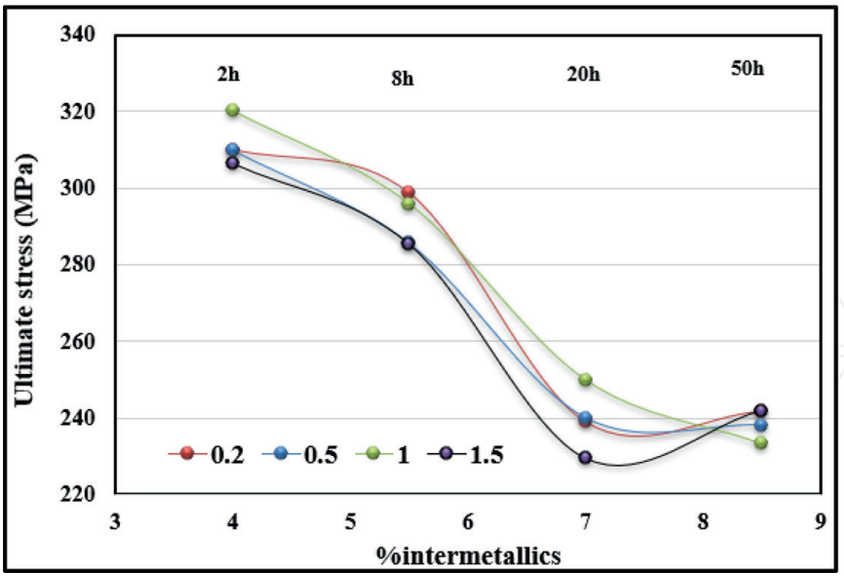

Figure 10.
Effect of aging time at 180°C and Ce concentration on the ultimate tensile strength of A413.1 alloy.

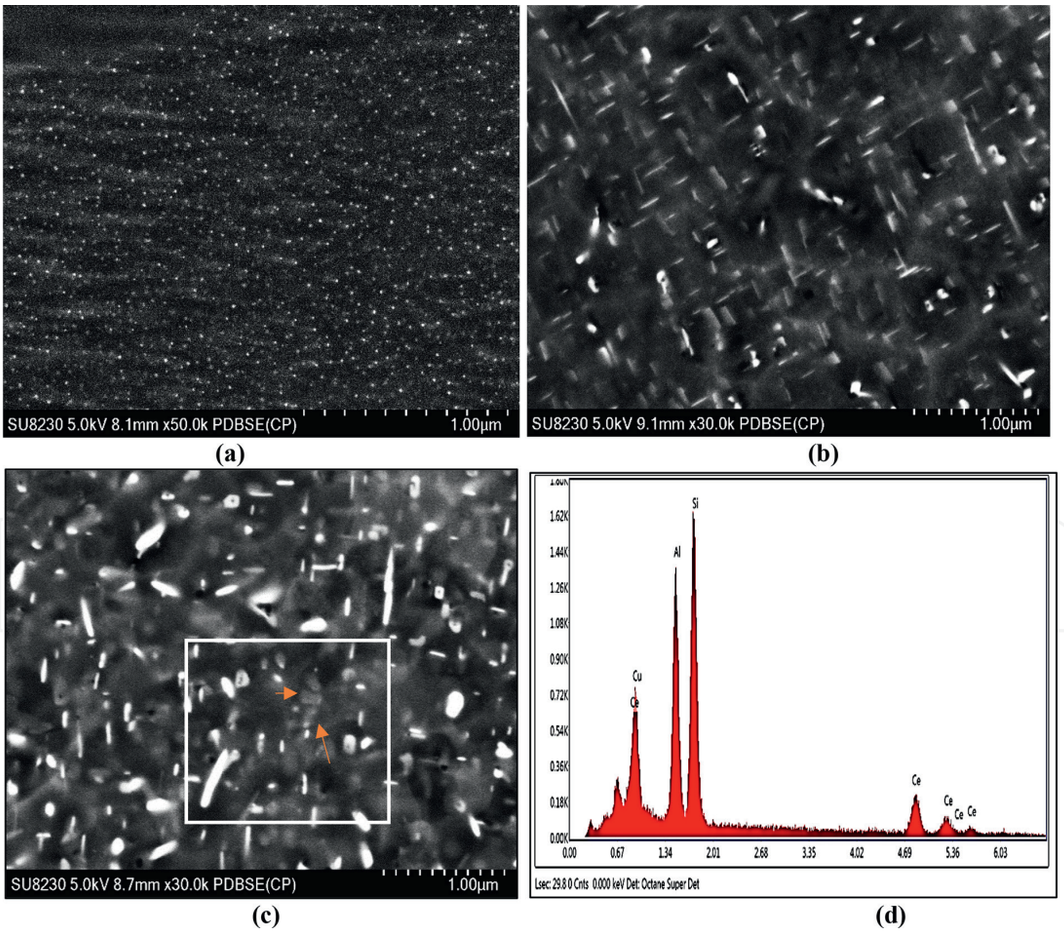

Figure 11.
Precipitation in A413.1 alloy containing 1.5%Ce and aged at 180°C: (a) 2 h, (b) 8 h, (c) 50 h, and (d) EDS spectrum corresponding to the white square in (c).

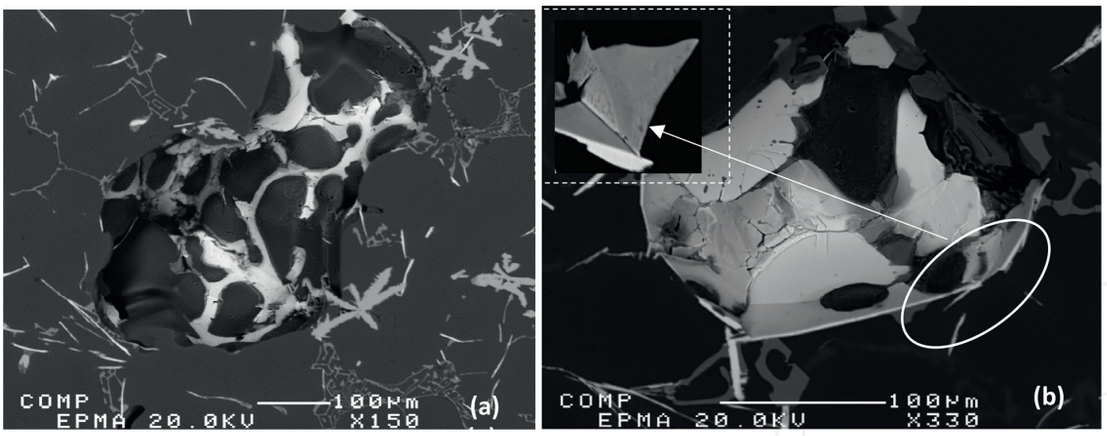

Figure 12.
Effect of RE-based intermetallics on porosity formation: (a) Ce and (b) La.

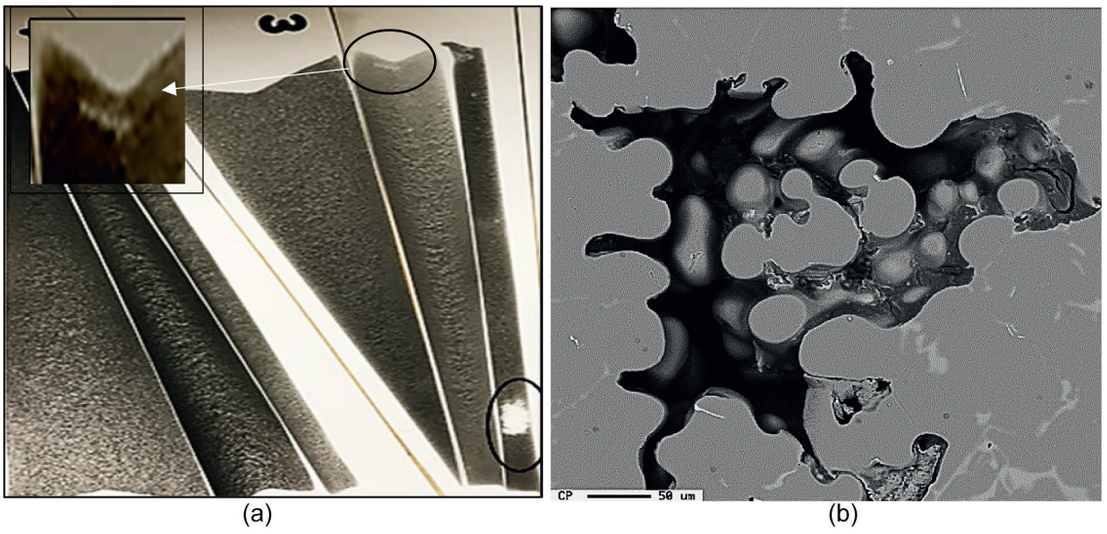

Figure 13.
(a) Radigraphs of castings made using variable metallic mold heated at 350°C. (b) Shrinkage cavities that resulted from the solidification of a hot zone.

pockets of liquid metal surrounded by solidified materials. As a result, during the solidification of these pockets, severe shrinkage cavities are formed, exemplified in **Figure 13(b)**.

Since the mold is open-face, severe shrinkage cavities would occur at the top of each casting as highlighted by the inset micrograph in **Figure 13(a)**. Also, oxide films may get trapped in the castings (SrO films), which would contribute to porosity concentration [36]. Thus, to minimize the error in evaluating porosity mainly due to RE, samples were sectioned from the middle of each casting as shown in **Figure 2(c)**. **Figure 14** depicts the effect of RE and (RE + Sr) on porosity percentage in castings at different titling angles. It should be mentioned here that the term (Ce + La) means addition of equal amounts of both elements, that is, double the amount of an individual element addition.

According to Mahmoud et al. [37–40], Ce reacts with La and other alloying elements mainly Al, Fe, Sr, and Cu. Although the added amount of RE is double that

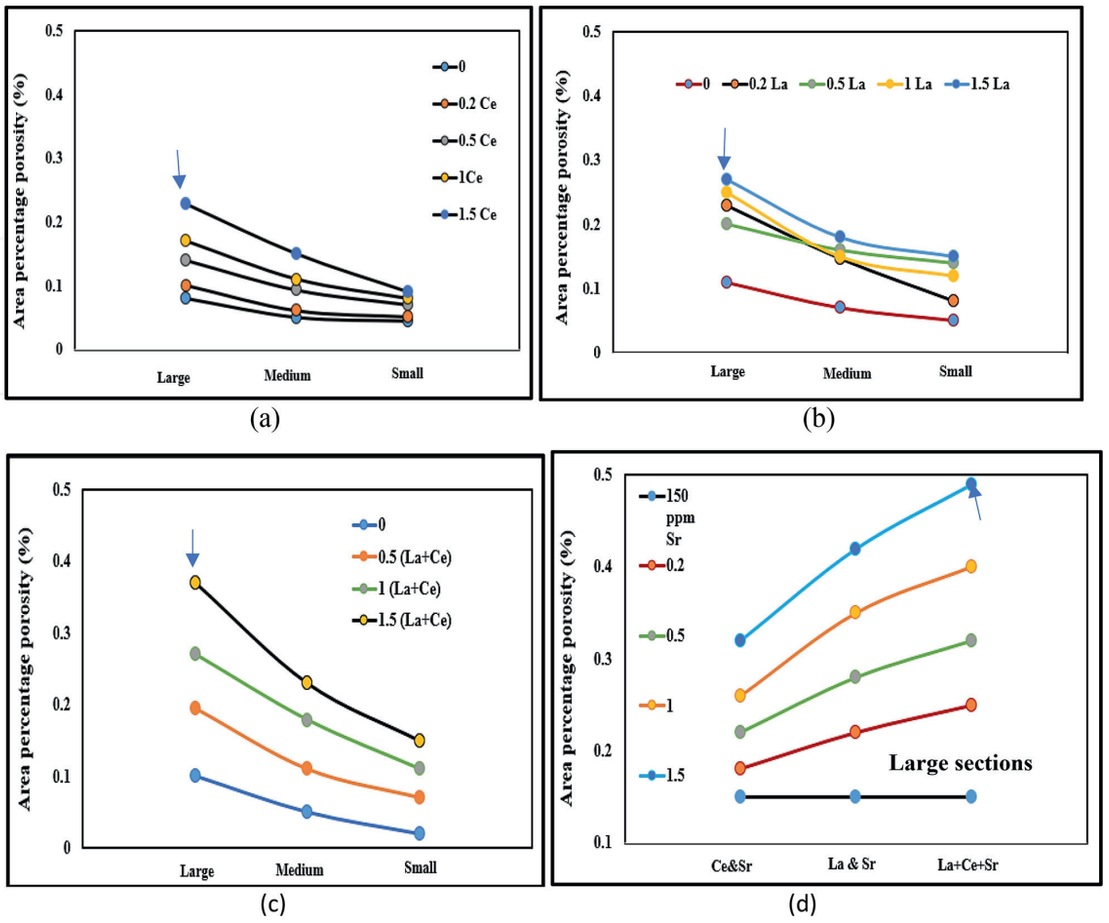

Figure 14.
Effect of RE on porosity percentage: (a) Ce, (b) La, (c) Ce + La, and (d) RE + Sr—arrows point to a large section (maximum % of porosity).

of a single element addition, the resulting volume fraction of intermetallics is higher than that obtained from individual elements but not necessarily double the volume fraction shown in **Figure 10**. **Figure 14(a)** and **(b)** display the variation in % of total porosity as a function of casting section and added RE. Both Ce and La addition in the same quantity produces the same pattern except for the addition of La, where it may result in a slightly higher value (0.28%) than that reported for Ce (0.22%) due to the difference in the morphology of the precipitated intermetallics, that is, platelets vs. star-like. Doubling the concentration—(La + Ce)—**Figure 14(c)** increased the % of porosity to about 0.42% (large sections). As shown in **Figure 14(d)**, treating the alloy with 150 ppm Sr led to a noticeable increase in % porosity, up to 0.5%, representing a mixture of porosity caused by RE and Sr.

In order to gain a better understanding of the data presented in **Figure 14**, a series of backscattered electron taken from large section samples is shown in **Figure 15** demonstrating the progressive increase in % porosity with the added elements. **Figure 15(a)** represents the base alloy revealing the absence of porosity, whereas **Figure 15(b)** of A413.1 alloy containing 1.5%La exhibits the appearance of scattered shrinkage cavities shown in areas marked A, B, and C. As presented in **Figure 5**, the maximum melting point of the present alloy containing 1.5%La is in the range of 575–580°C, which is much lower than the eutectic reactions depicted in **Figure 4**. Thus, it is reasonable to assume that La- and Ce-rich intermetallics may be precipitated prior

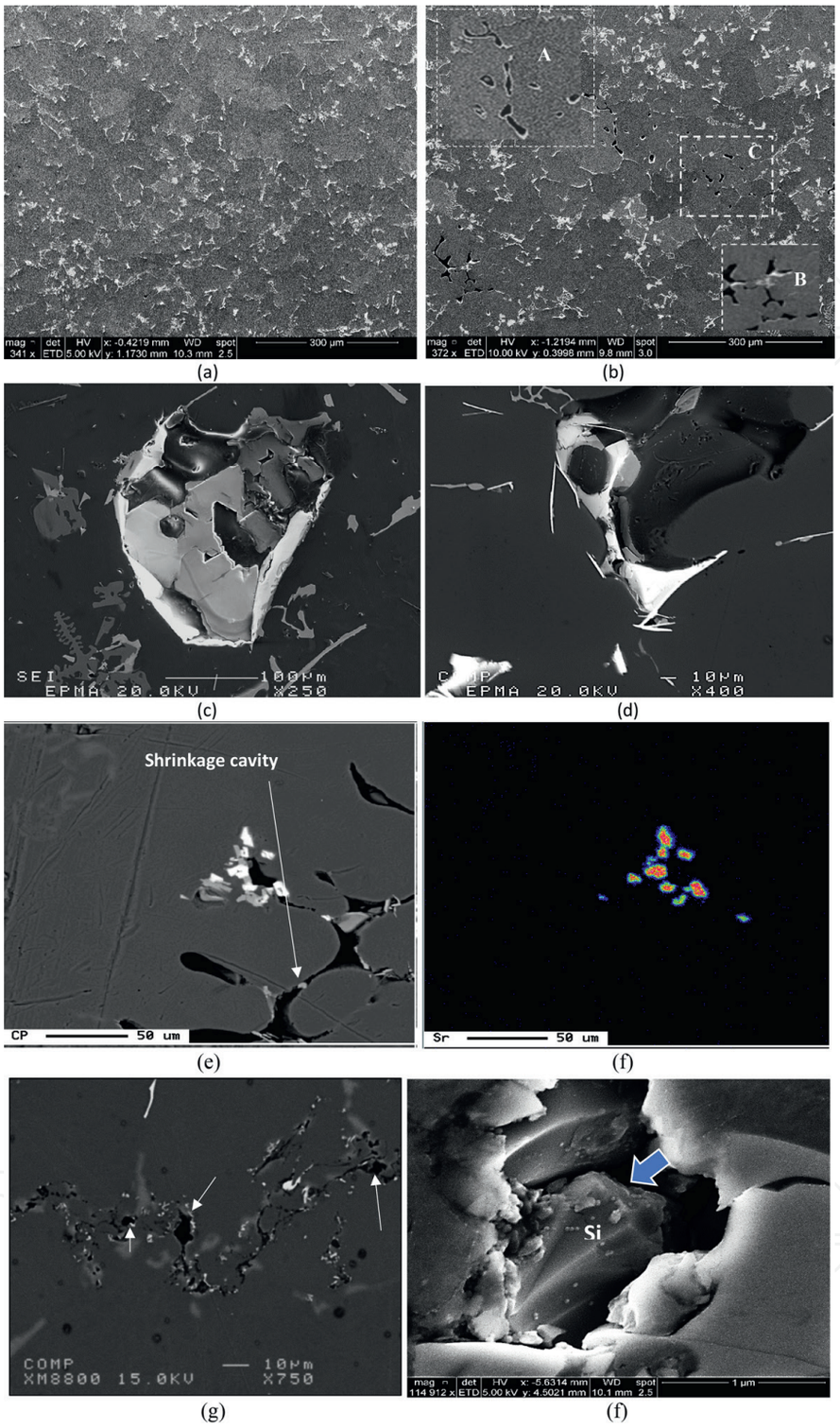

Figure 15.
Variation in porosity as a function of added RE (large sections): (a) no addition (b) 1.5% La, (c and d) 1.5% La + 1.5% Ce, (e) backscattered electron image of Sr addition, and (f) X-ray image of Sr in (e) (g) porosity associated with a long chain of oxide films-white arrow (f) morphology of an eutectic Si particle in a Sr-modified alloy—blue arrow.

to the formation of the α-Al network, leading to blocking the flow of liquid metal and hence explaining the large pore shown in **Figures 15(c)** and **(d)**. **Figure 15(e)** and **(f)** are good examples of precipitation of Sr-rich components in the aluminum matrix in

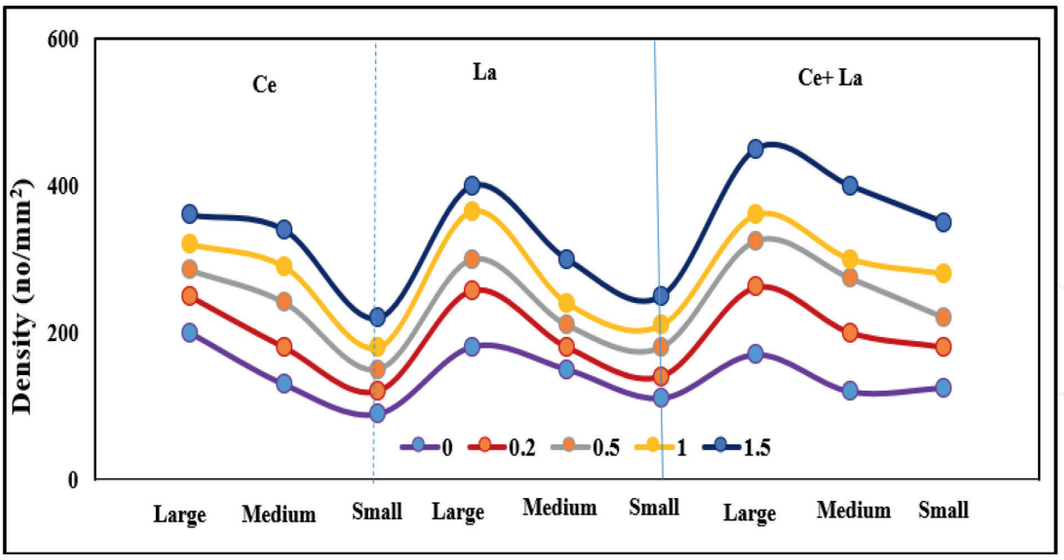

Figure 16.
Variation of density of porosity as a function of casting angle and added RE.

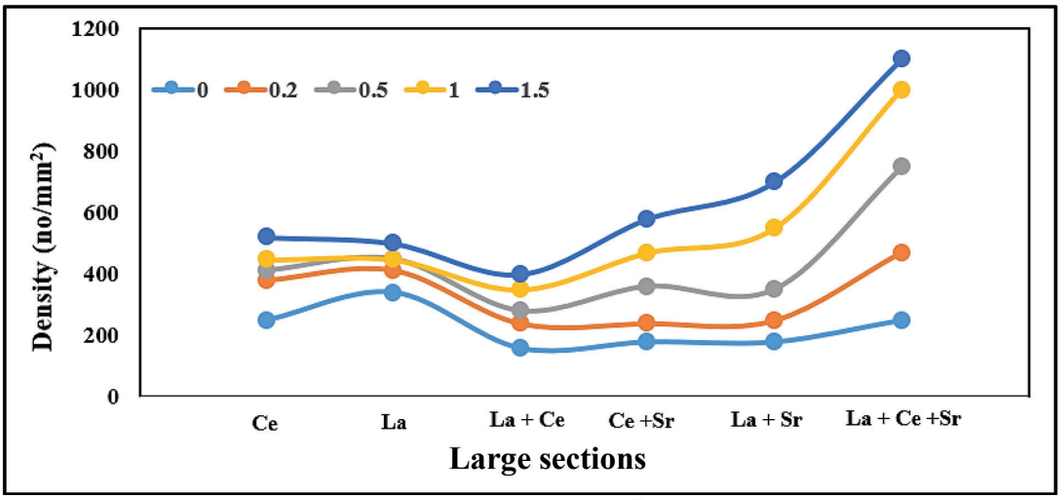

Figure 17.
Variation of density of porosity as a function of added RE and Sr.

the vicinity of large shrinkage cavities. Since there was no filtering, oxides can easily slip into the melt and create fine pores along their lengths as displayed in **Figure 15(g)**. An example of a modified Si particle in Sr treated alloy is given in **Figure 15(f)**.

Another parameter to be considered is the density of porosity caused by addition of the above elements as illustrated in **Figure 16**. The curve is divided into three blocks separated by thin broken lines. In each case, the density systematically increases as the mold angle increases, and the total amount of the added RE (no modification was used) reaching a maximum of 420 pores/mm^2 (1.5%La + 1.5%Ce, large angle). With the addition of 150 ppm Sr into the molten metal, a significant steady increase took place with the increase in the added materials reaching almost 1100 pores/mm^2—**Figure 17**, which is almost three times what was observed in **Figure 16**.

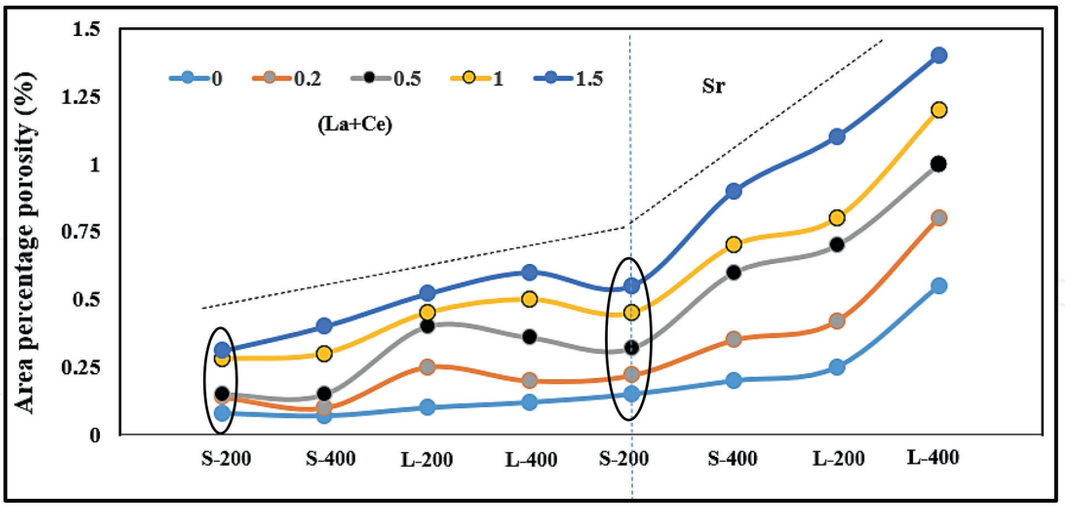

Figure 18.
Variation of area percentage porosity as a function of mold temperature, sample section, and RE.

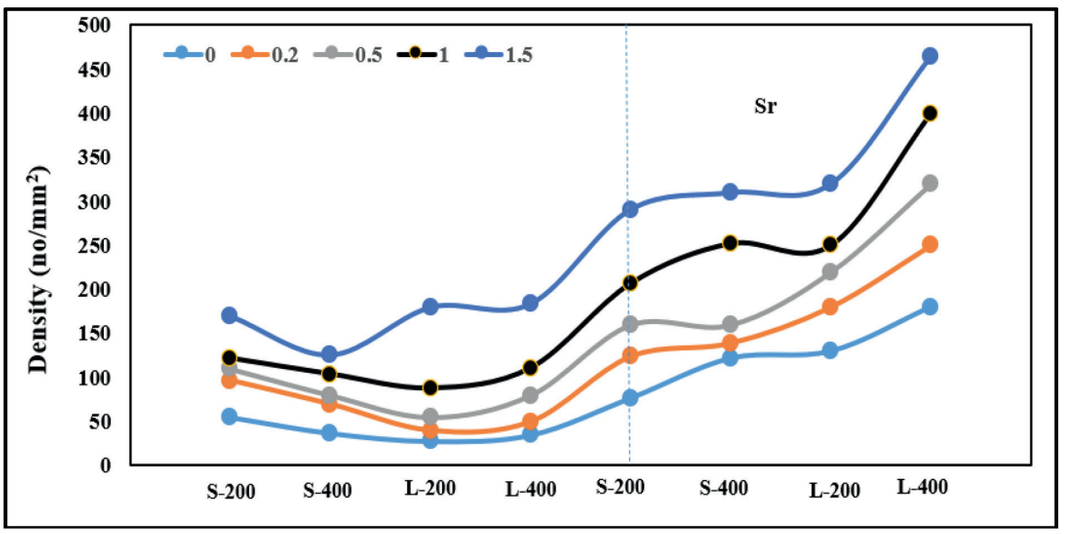

Figure 19.
Variation of pore density as a function of mold temperature, sample section, and RE.

3.3 Step-like metallic mold

As shown in **Figure 2(d)**, the step-like mold is made of thick walls (10 mm) with a pore cavity almost half the weight of the total casting to minimize occurrence of shrinkage cavities within the casting itself. Also, 1 mm from the top of sectioned samples was removed to avoid any possibility of interfering with casting shrinkage cavities with those resulting from the addition of RE (La + Ce). Both **Figures 18** and **19** reveal that aside from the increase of the parameter with the amount of introduced materials, a marked observation is that the slope of the curve is divided into two distinct angles when the melt was modified with Sr (150–180 ppm), in large sections, similar to those exhibited in **Figure 17**. The black circle in **Figure 18** shows a relatively high % porosity in small sections heated at 200°C, which may in part be due to reduction in the fluidity of molten metal in the non-modified alloys.

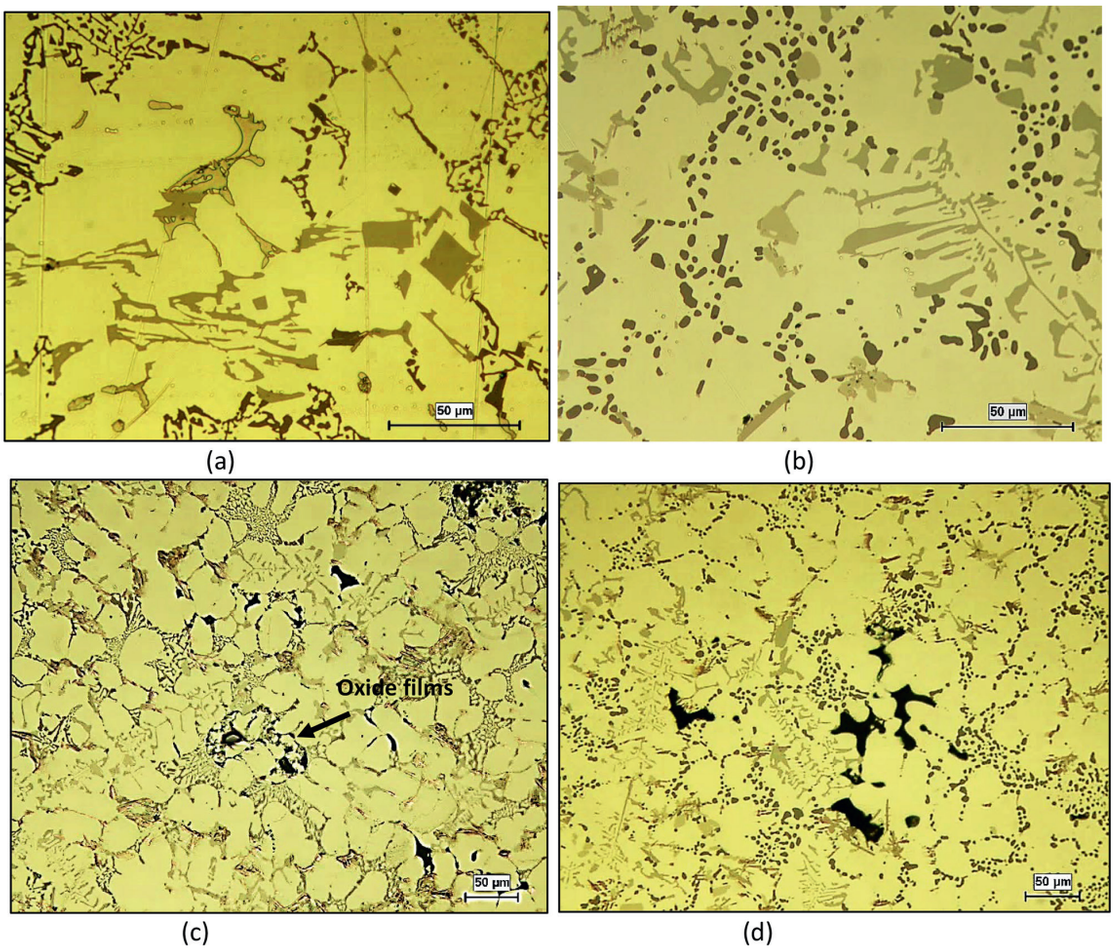

Figure 20.
Optical micrographs of RE and Porosity in large sections at 400°C: (a) precipitation of RE intermetallics in non-modified alloy, (b) precipitation of RE intermetallics in Sr-modified alloy, (c) porosity formation in non-modified alloy, and (d) porosity formation in Sr-modified alloy.

Figure 20 exhibits optical micrographs taken from large sections (400°C). **Figure 20(a)** and **(b)** show the precipitation of RE in non-modified and Sr-modified alloys, respectively-light gray phases (1.5%La +1.5%Ce). Since the molten metal was degassed prior pouring into the mold, most of the porosity is caused due to shrinkage. The pore size is small due to the use of a large filling cavity. Since no filtration was applied, some oxide films were able to pass through as shown in **Figure 20(c)**.

4. Conclusion

Based on the present results on the effect of additives and casting process on porosity formation in A413.1, the following conclusions may be drawn:

1. The addition of 1.5% rare earth metals (RE) largely increases the melting point of A413.1 alloy by 5-7 degrees due to the presence of new alloying elements, which is independent of Sr-modification.

2. RE reduces the eutectic temperature by about 3-4 degrees in non-modified alloys and 9°C in Sr-modified ones. There is no difference between 0.5% and 1.5% RE addition.

3. Increasing %RE has a marked deterioration on the alloy strength due to large volume fraction of insoluble intermetallics.

4. Due to the high affinity of Ce to react with Ti, the addition of 1.5%Ce would poison the grain refining. On the other hand, La has no reaction with Ti, and hence addition of 0.12%Ti + 1.5%La would lead to about 80% reduction in the alloy grain size.

5. Most of the observed porosities are caused by shrinkage, especially in Sr-treated alloys, regardless of the mold type.

6. The observation that some of the round pores are lined by layers of RE intermetallics may suggest that these intermetallics were precipitated in the liquid state blocking the flow of the liquid metals (maximum alloy melting point is about 580°C).

Author details

Ehab Samuel[1], Agnes M. Samuel[1], Victor Songmene[2] and Fawzy H. Samuel[1*]

1 Département des Sciences Appliquées, Université du Québec à Chicoutimi, Chicoutimi, QC, Canada

2 Department of Mechanical Engineering, École de Technologie Supérieure (ÉTS), Montréal, QC, Canada

*Address all correspondence to: fhsamuel@uqac.ca

References

[1] Humphries, Rare Earth Elements: The Global Supply Chain, Congressional Research Service. 2013

[2] Long KR, Van Gosen BS, Foley NK, Cordier D. The Geology of Rare Earth Elements, The Principal Rare Earth Elements Deposits of the United States, USGS Scientific. 2010

[3] King HM. REE - Rare Earth Elements and their Uses, Geology.com, Geoscience news and information. 2023

[4] Cordier DJ. Rare Earths. Mineral Commodity Summaries: United States Geological Survey; 2023

[5] Balaram. Rare earth elements: A review of applications, occurrence, exploration, analysis, recycling, and environmental impact, Geoscience Frontiers. Jul 2019;**10**(4):1285-1303

[6] Gursoy O, Timelli G. Lanthanides: A focused review of eutectic modification in hypoeutectic Al–Si alloys. Journal of Materials Research and Technology. 2020;**9**:8652-8666

[7] Jha K, Kumari A, Panda R, Kumar JR, Yoo K, Lee JY. Review on hydrometallurgical recovery of rare earth metals. Hydrometallurgy. 2016;**165**:2-26

[8] Tunsu C, Ekberg C, Foreman M, Retegan T. Studies on the solvent extraction of rare earth metals from fluorescent lamp waste using cyanex 923. Solvent Extraction and Ion Exchange. 2014;**32**:650-668. DOI: 10.1080/07366299.2014.925297

[9] Anastopoulos P, Bhatnagar A, Lima EC. Adsorption of rare earth metals: A review of recent literature. Journal of Molecular Liquids. 2016;**221**:954-962

[10] Miur T, Wada A. Precise purity analysis of high-purity lanthanum oxide by gravimetric analysis assisted with trace elemental analysis by inductively coupled plasma mass spectrometry. Frontiers in Chemistry. 2022;**10**:888636

[11] Abbasalizadeh A, Malfliet A, Seetharaman S, Sietsma J, Yang Y. Electrochemical extraction of rare earth metals in molten fluorides: Conversion of rare earth oxides into rare earth fluorides using fluoride additives. Journal of Sustainable Metallurgy. 2017;**3**:627-637. DOI: 10.1007/s40831-017-0120-x

[12] Zhou B, Li Z, Chen C. Global potential of rare earth resources and rare earth demand from clean technologies. Minerals. 2017;7(11):203. DOI: 10.3390/min7110203

[13] Zhu M, Jian ZY, Yang GC, Zhou YH. Effects of T6 heat treatment on the microstructure, tensile properties, and fracture behavior of the modified A356 alloys. Materials & Design. 2012;**36**:243-249

[14] Mousavi GS, Emamy M, Rassizadehghani J. The effect of mischmetal and heat treatment on the microstructure and tensile properties of A357 Al-Si casting alloy. Materials Science and Engineering a-Structural Materials Properties Microstructure and Processing. 2012;**556**:573-581

[15] Dang B, Jian ZY, Xu JF. Effects of rare-earth element addition and heat treatment on the microstructures and mechanical properties of Al-25% Si alloy. International Journal of Materials Research. 2017;**108**:269-274

[16] Zhang X, Wang ZH, Zhou ZH, Xu JM. Influence of rare earth (Ce and

La) addition on the performance of Al-3.0 wt%Mg alloy. Journal of Wuhan University of Technology-Materials Science Edition. 2017;**32**:611-618

[17] Xiao DH, Wang JN, Ding DY, Yang HL. Effect of rare earth Ce addition on the microstructure and mechanical properties of an Al–Cu–Mg–Ag alloy. Journal of Alloys and Compounds. 2003;**352**:84-88

[18] Xiao DH, Wang JN, Ding DY. Effect of minor cerium additions on microstructure and mechanical properties of cast Al – Cu – Mg – Ag alloy. Materials Science and Technology. 2004;**20**:1237-1240

[19] Tsai YC, Lee SL, Lin CK. Effect of trace Ce addition on the microstructures and mechanical properties of A356 (AL-7SI-0.35 Mg) aluminum alloys. Journal of the Chinese Institute of Engineers. 2011;**34**:609-616

[20] Voncina M, Kores S, Mrvar P, Medved J. Effect of Ce on solidification and mechanical properties of A360 alloy. Journal of Alloys and Compounds. 2011;**509**:7349-7355

[21] Voncina M, Mrvar P, Petric M, Medved J. Microstructure and grain refining performance of Ce on A380 alloy. Journal of Mining and Metallurgy, Section B: Metallurgy. 2012;**48**:265-272

[22] Li QL, Xia TD, Lan YF, Zhao WJ, Fan L, Li PF. Effect of rare earth cerium addition on the microstructure and tensile properties of hypereutectic Al-20%Si alloy. Journal of Alloys and Compounds. 2013;**562**:25-32

[23] Ye LY, Gu G, Liu J, Jiang HC, Zhang XM. Influence of Ce addition on impact properties and microstructures of 2519A aluminum alloy. Materials Science and Engineering: A. 2013;**582**:84-90

[24] Yii SLJ, Anas NM, Ramdziah MN, Anasyida AS. Microstructural and mechanical properties of Al-20%Si containing cerium. Procedia Chemistry. 2016;**19**:304-310

[25] Ouyang ZY, Mao XM, Hong M. Multiplex modification with rare earth elements and P for hypereutectic Al-Si alloys. Journal of Shanghai University (English Edition). 2007;**11**:400-402

[26] Tsai YC, Chou CY, Lee SL, Lin CK, Lin JC, Lim SW. Effect of trace La addition on the microstructures and mechanical properties of A356 (Al–7Si–0.35 Mg) aluminum alloys. Journal of Alloys and Compounds. 2009;**487**:157-162

[27] Hosseinifar M, Malakhov DV. The sequence of intermetallics formation during the solidification of an Al-Mg-Si alloy containing La. Metallurgical and Materials Transactions A. 2010;**42**:825-833

[28] Mahmoud MG, Samuel AM, Doty HW, Valtierra S, Samuel FH. Effect of rare earth metals, Sr, and Ti addition on the microstructural characterization of A413.1 alloy. Advances in Materials Science and Engineering. 2017;**2017**:12. DOI: 10.1155/2017/4712946

[29] Alkahtani SA, Elgallad EM, Tash MM, Samuel AM, Samuel FH. Effect of rare earth metals on the microstructure of Al-Si based alloys. Materials. 2016;**9**(1):45

[30] Elgallad EM, Doty HW, Alkahtani SA, Samuel FH. Effects of La and Ce addition on the modification of Al-Si based alloys. Advances in Materials Science and Engineering. 2016;**2016**:13

[31] Cacciamani G, Ferro R. Thermodynamic modeling of some aluminum-rare earth binary systems:

Al-La, Al-Ce and Al-Nd. Calphad. 2001;**25**(4):583-597

[32] Nabawy AM, Samuel AM, Alkahtani SA, Abuhasel KA, Samuel FH. Role of cerium, lanthanum, and strontium additions in an Al–Si–Mg (A356) alloy. International Journal of Materials Research. 2016;**107**(5):446-458

[33] Ferraro S, Fabrizi A, Timelli G. Evolution of sludge particles in secondary die-cast aluminum alloys as function of Fe, Mn and Cr contents. Materials Chemistry and Physics. 2015;**153**(1):168-179

[34] Dong X, Ji S. Si poisoning and promotion on the microstructure and mechanical properties of Al–Si–Mg cast alloys. Journal of Materials Science. 2018;**53**:7778-7792

[35] Weiler JP. A review of magnesium die-castings for closure applications. Journal of Magnesium and Alloys. 2019;**7**(2):297-304. DOI: 10.1016/j.jma.2019.02.005

[36] Samuel AM, Ammar HR, Zedan Y, Doty HW, Samuel FH. Effect of Ca–Sr–Mg and Bi–Sr–Mg interactions on the microstructural characterization and tensile properties of B319 alloy. International Journal of Metalcasting. 2022;**16**(4):1940-1959

[37] Mahmoud MG, Zedan Y, Samuel AM, Songmene V, Samuel FH. The use of rare earth metals in Al–Si–Cu casting alloys. International Journal of Metalcasting. 2022;**16**(2):535-552

[38] Mahmoud, M.G., Y. Zedan, A.M. Samuel, V. Songmene, H.W. Doty, and F.H. Samuel, Applications of Rare Earth Metals in Al-Si Cast Alloys, in Advances in High-Entropy Alloys - Materials Research, Exotic Properties and Applications. IntechOpen; 2021

[39] Mahmoud MG, Samuel AM, Doty HW, Samuel FH. Formation of Rare Earth Intermetallics in Al–Cu Cast Alloys, in Light Metals Symposium held at the 149th Annual Meeting and Exhibition. San Diego; United States: TMS 2020; 2020. pp. 241-246

[40] Makhlouf MM, Apelian D. Casting Characteristics of Aluminum Die Casting Alloys. Vol. No. DOE/ID/13716. Worcester, Massachusetts, USA: Worcester Polytechnic Institute; 2002